

See discussions, stats, and author profiles for this publication at: <https://www.researchgate.net/publication/356997979>

Simulation and Uncertainty Quantification of Electron Beams in Active Spacecraft Charging Scenarios

Article in *Journal of Spacecraft and Rockets* · December 2021

DOI: 10.2514/1.A35190

CITATIONS

9

READS

114

3 authors:



Álvaro Romero-Calvo
Georgia Institute of Technology

50 PUBLICATIONS 217 CITATIONS

[SEE PROFILE](#)



Gabriel Cano-Gómez
Universidad de Sevilla

22 PUBLICATIONS 130 CITATIONS

[SEE PROFILE](#)



Hanspeter Schaub
University of Colorado Boulder

266 PUBLICATIONS 7,789 CITATIONS

[SEE PROFILE](#)

Simulation and uncertainty quantification of electron beams in active spacecraft charging scenarios*

Álvaro Romero-Calvo [†]

Department of Aerospace Engineering Sciences, University of Colorado Boulder, CO, 80303, United States

Gabriel Cano-Gómez[‡]

Departamento de Física Aplicada III, Universidad de Sevilla, Sevilla, 41092, Spain

Hanspeter Schaub [§]

Department of Aerospace Engineering Sciences, University of Colorado Boulder, CO, 80303, United States

Novel active sensing methods have been recently proposed to measure the electrostatic potential of non-cooperative objects in geosynchronous equatorial orbit and deep space. Such approaches make use of electron beams to excite the emission of secondary electrons and X-Rays and infer properties of the emitting surface. However, the detectability of secondary electrons is severely complicated in the presence of complex charged bodies, making computationally efficient simulation frameworks necessary for in-situ potential estimation. The purpose of this paper is twofold: firstly, to introduce and test a quasi-analytical, uncoupled, and computationally efficient electron beam expansion and deflection model for active charging applications; and secondly, to characterize the uncertainty in the beam-target intersection properties, which condition the measurement of secondary electrons. The results show that a combination of secondary electrons and X-ray methods is highly desirable to yield a robust and accurate measure of the potential of a target spacecraft.

Nomenclature

α	= electrode rotation angle, rad
β	= velocity ratio
\mathcal{B}	= nondimensional external magnetic flux density
B	= external magnetic flux density, T
b	= internal magnetic flux density, T

*An early version of this work was presented at the AIAA Scitech 2021 Virtual Forum with AIAA paper number 2021-1540 on 11–15 & 19–21 January 2021.

[†]Graduate Research Assistant, Department of Aerospace Engineering Sciences, University of Colorado Boulder, alvaro.romerocalvo@colorado.edu, AIAA Student Member. Corresponding author.

[‡]Associate Professor, Departamento de Física Aplicada III, Universidad de Sevilla, gabriel@us.es.

[§]Professor, Glenn L. Murphy Chair in Engineering, Department of Aerospace Engineering Sciences, University of Colorado Boulder, hanspeter.schaub@colorado.edu, AIAA Member.

C	= body capacitance, F
c	= speed of light, ms^{-1}
δ	= initial beam divergence angle, rad
ϵ_0	= permittivity of free space, Fm^{-1}
\mathcal{E}	= nondimensional external electric field
E	= external electric field, V/m
E_j	= external electric field of sphere j , V/m
E_b	= beam energy, J
e	= internal electric field, V/m
\mathcal{F}	= nondimensional external Lorentz's force
F	= external Lorentz's force, N
f	= internal Lorentz's force, N
γ	= Lorentz factor
I_b	= beam current intensity, A
I_0	= reference beam current intensity, A
k_c	= Coulomb constant, Nm^2C^{-2}
L_c	= mean spacecraft separation, m
μ_0	= permeability of free space, Hm^{-1}
m_e	= electron mass, kg
n	= volume density distribution of electrons, m^{-3}
p	= position vector, m
q	= spheres charge vector, C
q_i	= sphere i charge, C
q	= electron charge, C
\mathcal{R}	= dimensionless ratio
R_b	= beam radius, m
R_i	= sphere i radius, m
r	= radial beam coordinate, m
$r_{i,j}$	= distance between sphere i and j , m
$[S]$	= elastance matrix, F^{-1}
s	= arc parameter along beam centroid, m
θ	= beam deflection angle, rad

τ	= nondimensional time
t	= time, s
\mathbf{v}	= nondimensional electron velocity
\mathbf{V}	= spheres potential vector, V
V	= potential, V
V_i	= sphere i potential, V
v	= electron velocity, ms ⁻¹
v_z	= beam propagation velocity, ms ⁻¹
\mathbf{x}	= nondimensional inertial position
x	= inertial position, m
$\{\mathbf{u}_r, \mathbf{u}_\psi, \mathbf{u}_z\}$	= beam reference system
$\{\hat{\mathbf{x}}, \hat{\mathbf{y}}, \hat{\mathbf{z}}\}$	= global reference system

Subindices:

f	= final
\perp	= perpendicular to trajectory
ref	= reference value
tar	= target
ser	= servicer

Operators:

.	= scalar product
\times	= vector product

I. Introduction

The use of secondary electrons (SEs) [1] and X-rays [2, 3] has been recently proposed to touchlessly sense the electrostatic potential of objects in geosynchronous equatorial orbit or deep space. These methods, conceptualized in Fig. 1, make use of a servicing craft that directs a high-energy electron beam at the target of interest such that low-energy SEs and X-rays are emitted from the surface. Due to the charge unbalance induced by the electron beam, the SEs are accelerated toward the servicing craft, arriving with an energy equal to the potential difference between both bodies. The servicing craft measures the electron and photon energy spectrum and, knowing its own potential with respect to the ambient space plasma, infers the potential of the target [4]. This technology may find application in the electrostatic

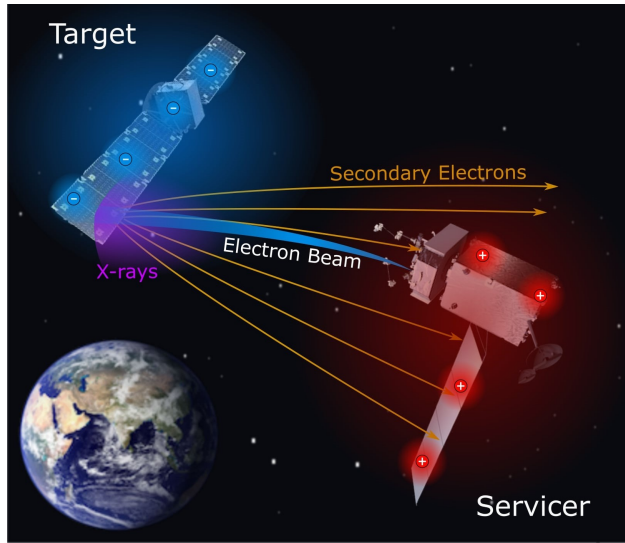


Fig. 1 Conceptual representation of the SEE- and X-Ray active spacecraft potential sensing methods.

detumbling [5] and reorbiting [6–8] of debris, Coulomb formations [9], material identification, and the mitigation of electrostatic perturbations during rendezvous, docking, and proximity operations [10, 11], among others. Potential levels of the order of 10s of keV and beam currents of up to 1 mA are commonly employed in these scenarios [12].

The validation of SE- and X-ray-based touchless electrostatic potential sensing methods has been thoroughly addressed in vacuum chamber experiments with flat plates, which simplify experimental procedures and ease data interpretation [1, 3, 13]. However, a flat surface is not representative of a standard spacecraft, whose complex geometry leads to highly inhomogeneous electric fields and well-defined paths where SEs move. The detection of SEs at a servicing spacecraft is hence conditioned by the target’s geometry, relative position, and source region [14]. In fact, the intersection between the electron beam and the target object defines the area where SEs are generated, and so an appropriate electron beam propagation model is needed. Past missions have operated electron beams in space, with some examples being SCATHA [15] or the Electron Drift Instruments at GEOS [16], Freja [17], Cluster [18], and MMS [19]. Since beam repulsion effects were negligible or irrelevant in most cases, advanced electron beam models were not required. However, this may not be true in applications where the electrostatic repulsion plays a more relevant role.

Given the close dependence between beam steering and SE detection processes, the quantification of the beam-target intersection position uncertainty becomes fundamental for the development of potential sensing technologies based on SEs and X-rays. The ability to focus the electron beam on a specific spot of the target may also find application in the identification of surface materials and the characterization of differentially-charged objects. In this regard, it should be noted that although spacecraft design best practices recommend all exterior surfaces to be connected to a common ground to prevent electrostatic discharges [20], arcing events are far from uncommon, particularly in old spacecraft [21–24]. Therefore, the success of these methods largely depends on the quantification and mitigation of the

uncertainty of the system, the implementation of robust remote sensing strategies, and the development of accurate and computationally efficient simulation frameworks that support such strategies.

This paper introduces a simplified and computationally efficient electron beam dynamics model in Sec. II, assesses its validity in active spacecraft charging scenarios in Sec. III, and quantifies the uncertainty in the properties of the beam-target intersection area in Sec. IV. Monte Carlo simulations are implemented after adopting the perspective of the servicing spacecraft, unveiling the contribution of each parameter to the uncertainty in the outputs by means of a FAST sensitivity analysis.

II. Electron beam model

A. Context and strategy

Existing electron beam models may be divided into two families: those that fully implement the space-charge effects induced by the beam, and those that ignore such interaction [25]. In the former, the electric field depends on the trajectory of the particles and is hence computed by solving Poisson's equation in the simulation domain, leading to accurate results but large computational costs. Particle-In-Cell (PIC) simulations are commonly employed for this purpose, and have been widely used to study the injection and long-term propagation of electron beams in plasma environments [26–30]. Charged Particle Optics (CPO*) Boundary Element Method (BEM) [31] in combination with the space-charge cell and tube methods [32] has also been applied to all sorts of electrostatic problems [33]. In the models that ignore space-charge effects, on the contrary, the particle trajectories are propagated under the unperturbed electrostatic potential generated by the electrodes. Some representative approaches are SIMION's Coulombic and Beam repulsion models, that approximate the beam expansion dynamics by computing the electrostatic repulsion forces in the beam cross-section at each time step [25]. Simplified analytical results for the beam expansion process can also be found in the literature [34].

The appropriateness of a certain beam model depends on its scenario of application. In the active spacecraft charging problem, servicer and target spacecraft are separated a few 10s of meters and employ focused electron beams of 10s of kV. This implies that the beam will deflect only slightly before reaching the target. In fact, the short propagation distance makes it remain in the *initial expansion phase*, where the beam density is much larger than the GEO plasma density and the expansion dynamics are driven by the radial electric field in the beam cross section [35]. With GEO Debye lengths of 100-1000 m, plasma interactions can be safely ignored, but the beam evolution is determined by the electric field from nearby charged bodies.

A solution that can be regarded as an intermediate approach between the analytical expansion equations described by Humphries in Ref. 34 and SIMION's repulsion models [25] is subsequently presented. By taking advantage of the particular active spacecraft charging environment, a simplified framework of analysis that uncouples electron

*<https://simion.com/cpo/>. Consulted on: 06/01/2021

beam expansion and deflection processes is developed and combined with the Multi-Spheres Method (MSM) for the estimation of electric fields [36]. The result is a computational efficient but accurate particle-tracing-like model that can be integrated in an onboard flight algorithm. This is highly desirable for the applications here considered, as discussed in Sec. IV.

B. Physical model

The propagation of electron beams in space is subject to several internal and external electromagnetic interactions. The quasi-analytical physical model here presented assumes (i) negligible space-charge effects, (ii) small beam deflection angles θ , (iii) small radial expansion, (iv) axisymmetric distribution of geometry and loads within the beam cross-section, and (v) negligible plasma interactions.

The first two assumptions are key for developing a computationally efficient simulation framework, because they uncouple the beam-electrode system and the expansion and deflection processes. As explained in Sec. IV.A, small beam deflection angles are produced when the potential difference between servicer and target spacecraft is significantly smaller than the electron beam energy. This is the case of interest for remote sensing applications; otherwise, the beam may be deflected enough to completely avoid the target. The third and fourth assumptions reduce the cross-section electrostatic surface integrals to one dimension by allowing the implementation of an infinite cylindrical beam framework of analysis. Such approach is appropriate for small beam divergence angles and leads to large computational gains with respect to existing particle tracing simulations. Finally, and since the separation between servicer and target spacecraft is of the order of 10s of meters, which represents a fraction of the GEO Debye length of 100-1000 m, the electron beam dynamics can be reasonably studied without taking into account complex plasma interactions.

C. Mathematical model

In what follows, the deflection of the beam is assumed to be produced by the electromagnetic environment, while its expansion is a consequence of the distribution of charge in the beam cross-section and the initial beam divergence angle. The model simultaneously and independently addresses both problems by integrating the trajectories of the beam centroid (deflection) and a series of electrons distributed along the axisymmetric beam cross-section (expansion). In both cases, Lorentz's force defines the electromagnetic force on each particle through

$$\mathbf{F} = q(\mathbf{v} \times \mathbf{B} + \mathbf{E}), \quad (1)$$

with q and \mathbf{v} being the charge and velocity of the electron, and \mathbf{B} and \mathbf{E} denoting the magnetic flux density and electric field, respectively. The relativistic change in momentum of the particle is given by the balance

$$\frac{d(\gamma m_e \mathbf{v})}{dt} = \mathbf{F}, \quad (2)$$

where m_e is the mass of the electron, $\gamma = (1 - \beta^2)^{-1/2}$ is the Lorentz factor, $\beta = v/c$, c is the speed of light, and the time derivative is inertial. The position \mathbf{x} in the inertial reference frame is computed as

$$\frac{d\mathbf{x}}{dt} = \mathbf{v}. \quad (3)$$

It should be noted that, in accordance with the special theory of relativity, the inertia of a particle with respect to a reference frame depends on its speed with respect to such frame. Consequently, the term γm_e defines the apparent mass of the particle.

For the sake of clarity, the *internal* fields, that drive the expansion problem, are subsequently denoted by lowercase variables, while the *external* fields, that determine the deflection dynamics, are given by uppercase letters.

1. Expansion of cylindrical electron beams

In the beam expansion problem, the radial trajectories of a set of electrons are integrated at different radii of the beam cross-section using Eqs. 1-3. The internal electromagnetic fields and forces generated by axisymmetric cylindrical beams must consequently be computed. This is done under the infinite length approximation, leading to good estimates when the characteristic longitudinal (propagation) distance is much larger than the characteristic radius of the beam. The main advantage of this approach is the large reduction in computational cost achieved by expressing a 3D problem in the axisymmetric domain.

Axisymmetric cylindrical beams generate radial electric and azimuthal magnetic fields. The first is readily derived from Gauss's law, resulting in [34]

$$\mathbf{e}(r, t) = \frac{q}{\epsilon_0 r} \int_0^r dr' n(r', t) r' \mathbf{u}_r, \quad (4)$$

where ϵ_0 is the permittivity of free space, $n(r)$ denotes the volume density distribution of electrons, and $\{\mathbf{u}_r, \mathbf{u}_\psi, \mathbf{u}_z\}$ describes a cylindrical reference system centered in the axis of the beam and whose z component is aligned with the velocity. Similarly, Ampère's law gives the azimuthal magnetic field [34]

$$\mathbf{b}(r, t) = \frac{\mu_0 q v_z(t)}{r} \int_0^r dr' n(r', t) r' \mathbf{u}_\psi, \quad (5)$$

with μ_0 being the permeability of free space, and v_z the propagation velocity of the beam (assumed to be uniform in the cross-section). The modules of the electric and magnetic fields are related through $e = (c/\beta)b$. By applying Eq. (1) to these fields, the internal electromagnetic force becomes

$$\mathbf{f}(r, t) = \frac{q^2}{r \epsilon_0} (1 - \beta(t)^2) \int_0^r dr' n(r', t) r' \mathbf{u}_r, \quad (6)$$

where the z component of the force, cause by the radial expansion velocity, has been neglected. The magnetic and electric forces are related through $F_{\text{mag}} = -\beta^2 F_{\text{el}}$. For relativistic electron beams, both terms are approximately compensated ($\beta \rightarrow 1$), allowing long-distance transport at high current levels [34, 37].

The initial beam velocity profile is approximated in two steps. First, the velocity of propagation $v_z(0)$ is computed from the initial relativistic beam energy, $E_b = (\gamma - 1)m_0c^2$, by solving for γ and β . Then, the initial divergence angle δ , which is not caused by the electromagnetic repulsion between particles but by the optical configuration of the electron gun itself, is imposed as

$$\mathbf{v}(r, 0) \sim \frac{r\delta}{R_b} v_z(0) \hat{\mathbf{u}}_r + v_z(0) \hat{\mathbf{u}}_z, \quad (7)$$

where R_b is the beam radius and a quasi-collimated beam is assumed ($\delta \ll 1$). The initial electron density function, $n(r, 0)$, is modeled following a pre-defined statistical distribution (e.g. quasi-Gaussian, uniform, etc) that satisfies the electron beam current intensity I_b and energy E_b . The condition

$$\int_0^{R_b} dr' 2\pi r' n(r', t) = \frac{I_b}{qv_z(t)} \quad (8)$$

is then imposed at each time step to conserve the electron beam current. This expression assumes a uniform v_z component computed in a plane perpendicular to the axis of the beam, which is consistent with the small radial expansion assumption of the model. Uniform beams can be discretized with a single external electron in the axisymmetric beam cross-section, while more complex profiles (e.g. Gaussian) should employ a finer discretization to capture the evolution of the distribution. A convergence analysis should be carried out in each case; in particular, high-intensity beams require more points to accurately simulate the electromagnetic repulsion effect.

It should be noted that, although Eqs. 4-8 are given as a function of time (describing the movement of a particle), they are actually associated with a steady-state solution. Time is related to the arc parameter s along the beam centroid through $\delta s = v_z \delta t$. In a straight beam, $s = z$, and each of these expressions can be written in terms of the cylindrical coordinates r and z . The ratio β also changes depending on the beam propagation velocity, which is computed in the deflection problem independently of the expansion algorithm.

2. Deflection of cylindrical electron beams

The deflection of the beam is here represented by the trajectory of the centroid of the cross-section, which is integrated using Eqs. 1-3 for given external electric and magnetic fields. While the first is mainly produced by the potential difference between both spacecraft, the second is imposed by the magnetic environment.

The charge q of a conducting body is related to its capacitance C through $q = CV$, where V is the potential with respect to the ambient plasma. The identification of the zero potential with the ambient plasma is a common choice in the spacecraft charging community [38] that has been adopted in this work. If V is known, then the capacitance can be

used to determine the total charge of the conducting body, from which the electric field at distant points can be computed. However, objects in close proximity exhibit mutual capacitance effects [39] which must be accounted for to accurately determine the total charge, its distribution, and the nearby electric field. Capacitance is a function of the geometry of the system, but analytical solutions are only available for a limited number of shapes (such as spheres or round plates). Therefore, a numerical solution scheme must be used to find the capacitance of the system. The Method of Moments is generally employed for that purpose and, based on its solution, the Multispheres Method (MSM) has been developed as a computationally efficient alternative to approximate the resulting charge distribution [36, 40]. The MSM performs such approximation by discretizing the geometry using equivalent charged spheres [36, 40]. Given the potential on each sphere and its location with respect to the rest, the charge distribution is computed by solving the linear system

$$\begin{pmatrix} V_1 \\ V_2 \\ \vdots \\ V_n \end{pmatrix} = k_c \begin{bmatrix} 1/R_1 & 1/r_{1,2} & \dots & 1/r_{1,n} \\ 1/r_{2,1} & 1/R_2 & \dots & 1/r_{2,n} \\ \vdots & \vdots & \ddots & \vdots \\ 1/r_{n,1} & 1/r_{n,2} & \dots & 1/R_n \end{bmatrix} \begin{pmatrix} q_1 \\ q_2 \\ \vdots \\ q_n \end{pmatrix}, \quad \mathbf{V} = [\mathbf{S}]\mathbf{q}, \quad (9)$$

where $k_c = 1/(4\pi\epsilon_0)$ is the Coulomb constant, R_i is the radius of each sphere, $r_{i,j}$ is the distance between spheres i and j , and $[\mathbf{S}]$ denotes the elastance matrix [39], which is the inverse of the capacitance matrix. If both spacecraft are assumed to be conducting bodies in electrostatics equilibrium, each of them must have an equipotential surface, and so all V_i belonging to the same surface must equal. This assumption is appropriate for a GEO spacecraft since modern design specifications require all outer surfaces to be electrically connected [20], although it can be relaxed for differential charging studies. The charge vector \mathbf{q} constitutes a model of the charge distributions on the spacecraft, which allows calculating the electric field \mathbf{E} created by these distributions as the superposition of the one produced by each individual charge q_j , given by

$$\mathbf{E}_j(r) = \frac{q_j}{4\pi\epsilon_0 p^3} \mathbf{p}, \quad p \geq R_j, \quad (10)$$

where \mathbf{p} denotes the radial position vector, and R_j is the radius of the sphere. An arbitrary number of spheres can be placed and their radii adjusted to match the capacitance of the MSM to the true value.

In relation to the magnetostatic interaction, this work assumes an arbitrarily oriented GEO magnetic field of 100 nT. Its large characteristic length of variation ($\sim 10^3$ km), the small characteristic time of the beam deflection process ($\sim 10^{-6}$ s), and the small influence of the field in the problem under consideration justify its treatment as a fixed parameter.

3. Nondimensional formulation

The numerical conditioning of the electron beam expansion and deflection problem can be largely improved by employing a dimensionless formulation of Eqs. 1-3, which become

$$\mathcal{F} = (\mathbf{v} \times \mathcal{B} + \mathcal{E}), \quad (11)$$

$$\frac{d(\gamma \mathbf{v})}{d\tau} = \mathcal{F}, \quad (12)$$

$$\frac{dx}{d\tau} = \mathbf{v}, \quad (13)$$

where

$$\mathbf{x} = \frac{\mathbf{x}}{x_{\text{ref}}}, \quad \tau = \frac{t}{t_{\text{ref}}}, \quad \mathbf{v} = \frac{t_{\text{ref}}}{x_{\text{ref}}} \mathbf{v}, \quad \mathcal{B} = \frac{q_{\text{ref}} t_{\text{ref}}}{m_{\text{ref}}} \mathbf{B}, \quad \mathcal{E} = \frac{q_{\text{ref}} t_{\text{ref}}^2}{m_{\text{ref}} x_{\text{ref}}} \mathbf{E}, \quad \mathcal{F} = \frac{t_{\text{ref}}^2}{m_{\text{ref}} x_{\text{ref}}} \mathbf{F}. \quad (14)$$

The electron mass and charge are taken as a reference (m_{ref} , q_{ref}), with the characteristic time being $t_{\text{ref}} = 10^{-6}$ s. The characteristic length x_{ref} is equal to the initial electron beam radius R_b and the mean spacecraft separation L_c for the expansion and deflection processes, respectively. In other words, two different dimensionless problems are solved simultaneously.

4. Validity metrics

As noted in Sec. II.B, the analytical model introduced in this section is valid while the beam deflection angle

$$\theta = \arccos \left[\frac{\mathbf{v}(0) \cdot \mathbf{v}(t_f)}{|\mathbf{v}(0)| |\mathbf{v}(t_f)|} \right], \quad (15)$$

is small, with t_f denoting the final simulation time. The additional dimensionless parameter

$$\mathcal{R} = \frac{\gamma m v^2}{|q L_c (\mathbf{v} \times \mathbf{B} + \mathbf{E})_{\perp}|} = \frac{\gamma v^2}{|(\mathbf{v} \times \mathcal{B} + \mathcal{E})_{\perp}|} \quad (16)$$

is defined to describe the ratio between the instantaneous electromagnetic gyroradius and the characteristic spacecraft separation L_c , with \perp denoting the force component perpendicular to the electron trajectories and the different variables referring to the deflection problem. The metric \mathcal{R} reflects the influence of the electromagnetic environment on the trajectory of the centroid. A small value of \mathcal{R} implies that its gyroradius is comparable to the characteristic spacecraft separation, which ultimately leads to the focusing of the beam. The reader may visualize this scenario with a simple geometrical problem: if two identical circumferences are initially superposed and then separated slightly, two intersection points will be generated. The same happens with an electron beam when $\mathcal{R} \leq 1$. This effect is not contemplated in the model, which explains why \mathcal{R} (θ) must be significantly greater (smaller) than 1.

5. Numerical integration scheme

The integration of Eqs. 1-3 must conserve the total energy of the system. Common integrators, such as the standard 4th order Runge-Kutta (RK) method, carry a certain truncation error with each time step, resulting in unbounded divergences in the long term. This has made the Boris algorithm, which is an explicit, time-centered integrator that conserves the phase space volume and bounds the global energy error, the standard for particle physics simulations [41]. However, in short-term applications (like the one discussed in this manuscript) RK integrators still offer an accurate solution. In the simulations that follow, a variable-step, variable-order Adams-Basforth-Moulton PECE solver of orders 1 to 13 is implemented by means of Matlab's routine `ode113` [42], resulting in relative variations of total energy errors below 0.001%.

III. Performance analysis

A. Verification

Every model should be tested to verify its implementation, a step that is summarized here by independently focusing on the deflection and expansion processes. As described in Sec. II.C.5, the predicted trajectories pass the energy conservation test. Besides, they also match the analytical electron gyroradius and gyrofrequency in the presence of a constant magnetic field. Particle dynamics in combination with the MSM representation of charged bodies have been thoroughly addressed in previous works [43], leaving the beam expansion dynamics as the last module to be verified.

SIMION's documentation includes a case of analysis[†] where its Coulombic and Beam repulsion models are validated with coupled space-charge results from CPO [25]. The example consists on an isolated beam of 1 eV that originates in a 3 mm circle with an uniform distribution of 1000 electrons and a deflection angle of $\delta = -16.7^\circ$. The beam current is set as a multiple of the maximum value $I_0 = 3.47 \mu\text{A}$ sustained by the system, leading to the results depicted in Fig. 2. The same scenario is simulated with the beam model presented in Sec. II, showing an overall excellent agreement with SIMION. Small differences between both sets of results should be attributed to simplifying assumptions. For instance, the initial beam velocity profile in Eq. 7, leads to a set of particles with unequal kinetic energies. Although appropriate for small deflection angles (like the ones used in active spacecraft charging scenarios), this approximation performs worse with $\delta \gg 1$. However, while the computational cost of each SIMION simulation scales with the square of the number of particles [25], just a few trajectories are required by the proposed framework: the centroid, and a certain number of points in the axisymmetric cross-section that are employed to recompute the volume distribution of electrons. Since in this case such distribution is uniform, a single electron is needed to capture the evolution of the beam envelope; however, 50 particles are simulated for illustrative purposes. This computational advantage, together with the reduction of a complex problem to a small set of parameters, are the main advantage of the simplified model here introduced.

[†]The interested reader is referred to the `readme.html` file in the `examples/repulsion` folder of SIMION 2020

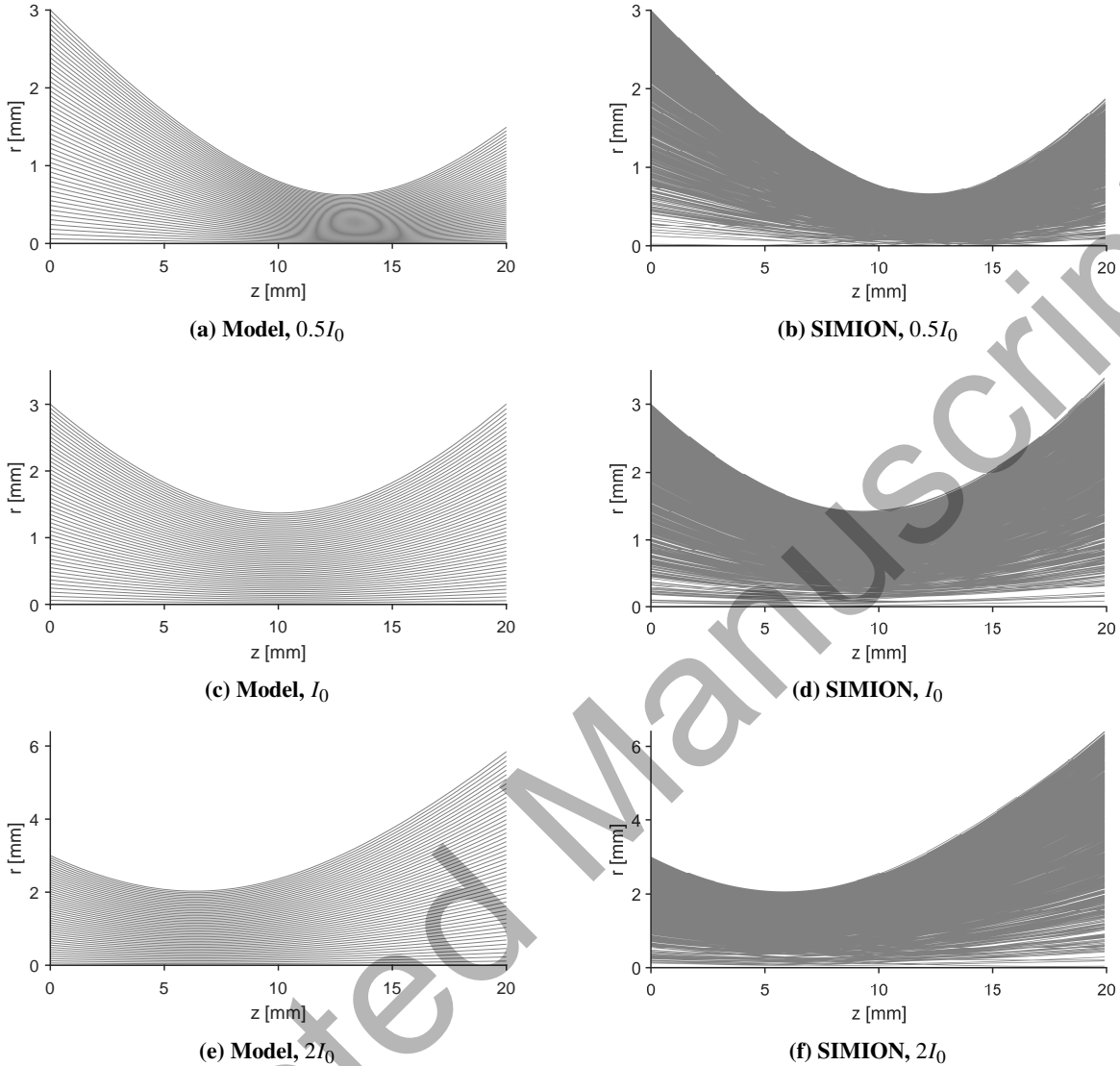


Fig. 2 Comparison between simulation framework and SIMION’s beam repulsion model [25] for $E = 1$ eV, $\delta = -16.7^\circ$, and $I_0 = 3.47\ \mu\text{A}$.

B. Validation

The physical mechanisms involved in the electron beam expansion and deflection processes have been very well understood for decades, and the validation of fundamental particle dynamics has consequently little technical value. On the contrary, future applications depend on the proper application of the model presented in Sec. II, which relies on a number of assumptions that limit its validity space. Provided that such assumptions are met, a computationally efficient and powerful analysis tool is obtained.

With the purpose of exploring the performance of the model in a worst-case scenario, the experimental setup shown in Fig. 3 is tested in the ECLIPS Space Environment Simulation Facility [44]. The assembly exposes an electron beam from a Kimball Physics EMG-4212D electron gun to the electric field generated by a charged spacecraft-like electrode

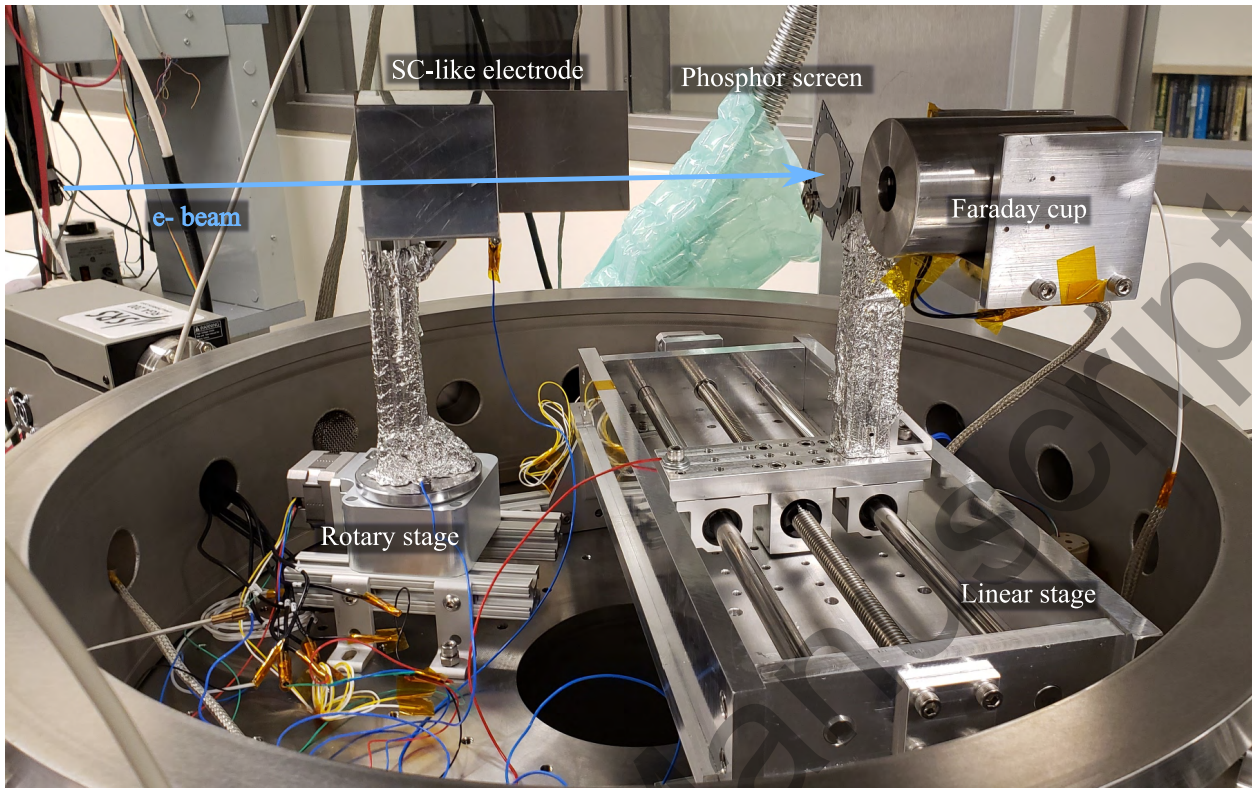


Fig. 3 Experimental setup inside the ECLIPS chamber

mounted on a rotary stage. The shape and location of the beam spot at approximately 35 cm from the gun orifice are observed with a 3.81 cm diameter rugged phosphor screen, and the spatial distribution is obtained with a Retarding Potential Analyzed (RPA) mounted on a linear stage. The beam is configured at 1 keV energy and 10 μA current, while the electrode is set at -100 to -500 V employing a Matsusada AU-30R1 high-voltage power supply. The electron flux at the RPA is measured with a Keithley 2400 multimeter. Finally, the system is automated by means of a LabView VI.

Figure 4 shows the beam spot profiles at the phosphor screen for electrode potentials ranging from -100 to -500 V. Because the gun orifice is slightly below the symmetry plane of the electrode, a voltage decrease leads to a slight downwards deflection. This is compensated with a fine tuning of the vertical gun deflection settings, which do not alter the horizontal position or shape of the spot. Figure 4a shows a ~ 13 mm diameter beam cross-section, which is considerably larger than the initial ~ 3 mm diameter beam. Tests with different beam current intensities give the same spot shape, which demonstrates that the expansion is not induced by the electrostatic repulsion between electrons, but by the initial beam spread angle δ . As the voltage decreases, the beam is deflected away from the electrode and its cross-section is elongated vertically. The spot shape is deformed significantly below -300 V, indicating the existence of small gyro radii with $\mathcal{R} \sim 1$. These observations are complemented with the electron flux distribution computed with the RPA in Fig. 5, where the narrowing process reduces the width of the flux peak and its amplitude. Based on the 0 V case, the spread angle is estimated to be $\delta \sim 2.5^\circ$. It should be noted that the apparent beam radius shown in Fig. 4a

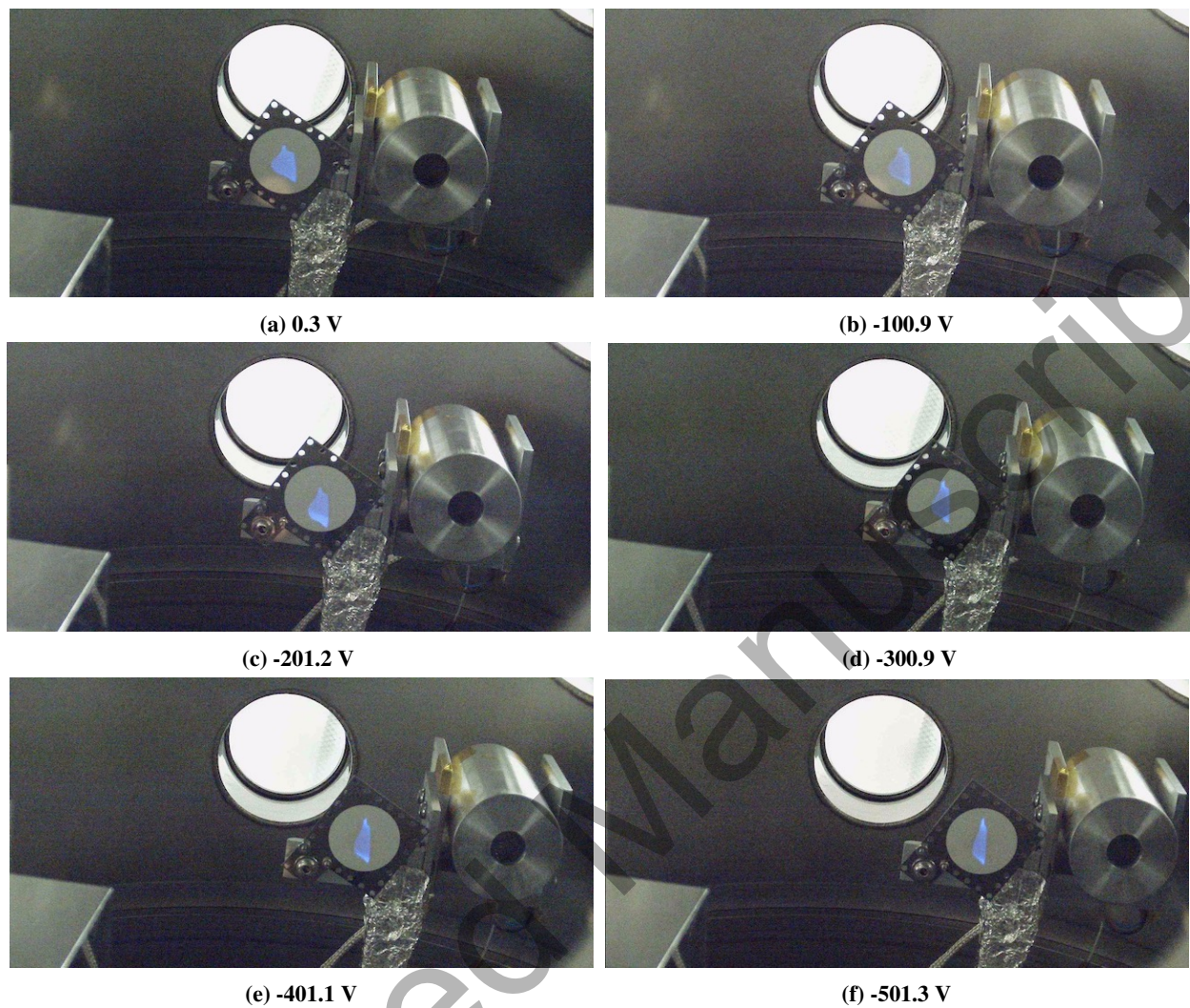


Fig. 4 Electron beam spot in the phosphor screen under different electrode potentials

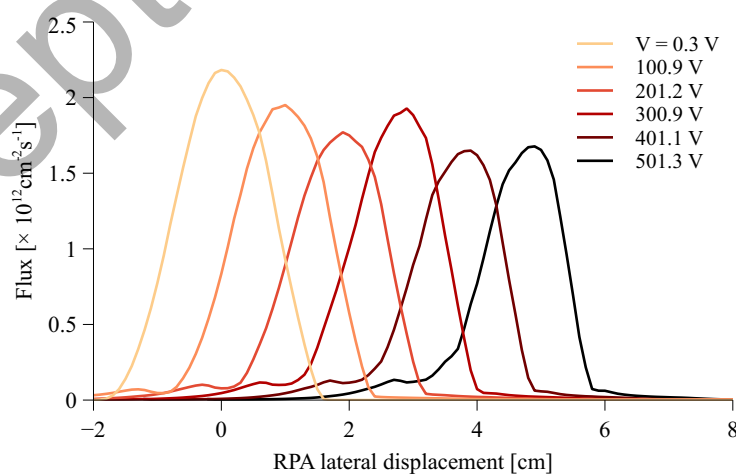


Fig. 5 Experimental electron flux distribution as a function of the applied electrode potential

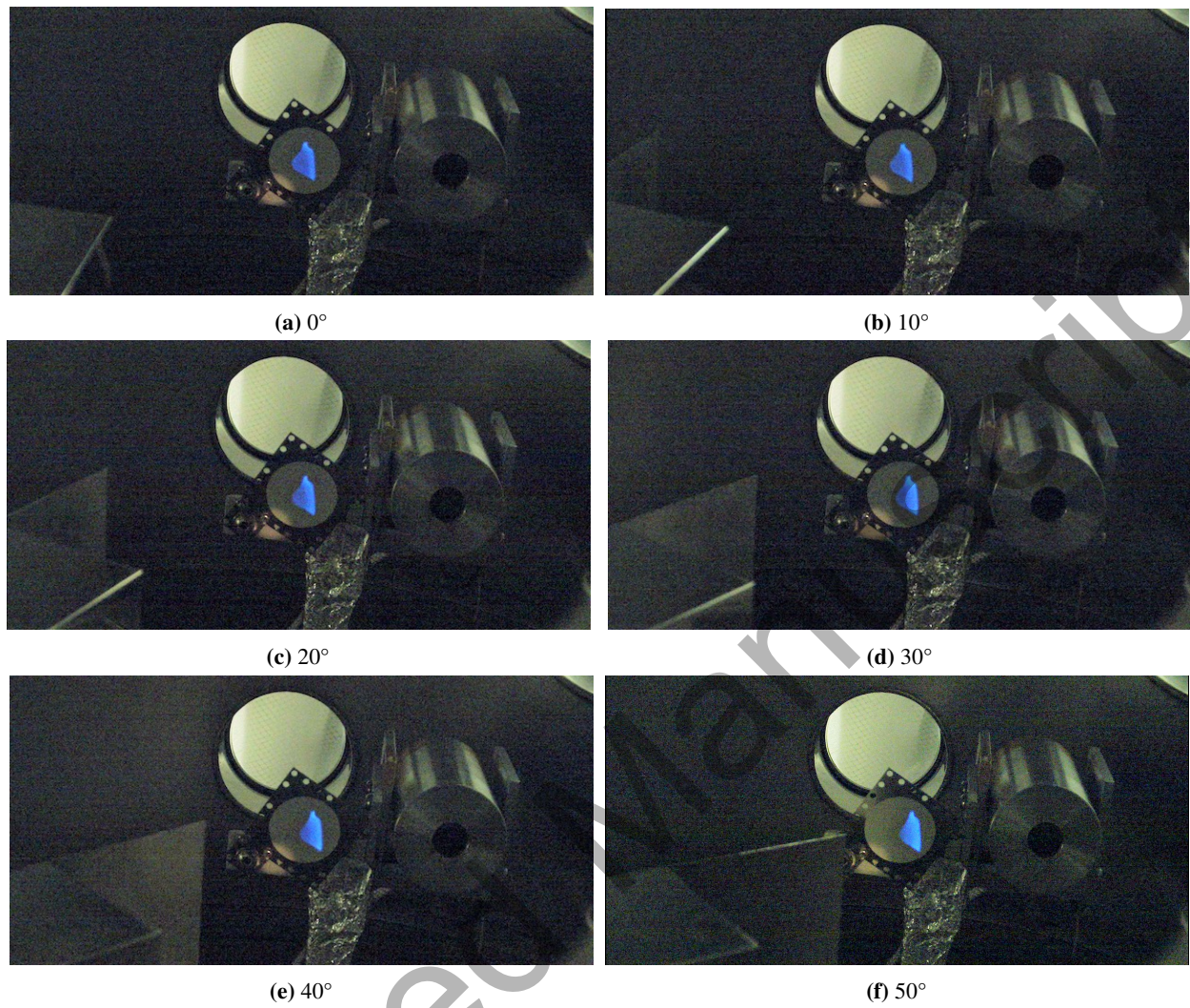


Fig. 6 Electron beam spot in the phosphor screen under different electrode rotation angles at -100 V

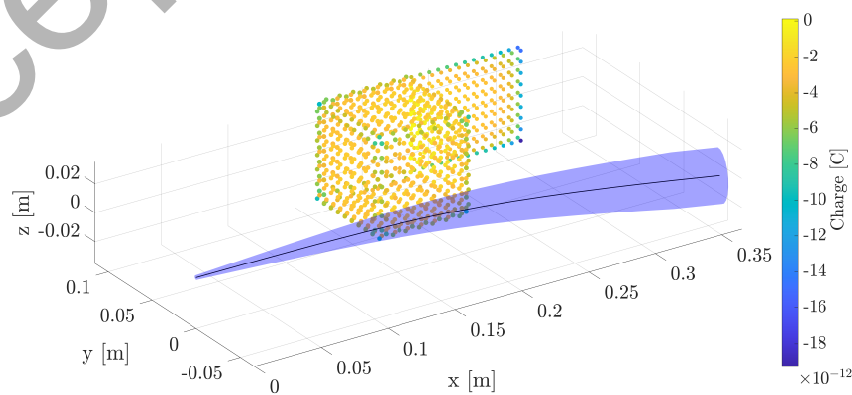


Fig. 7 MSM representation of the experimental setup with electron beam propagation at -500 V

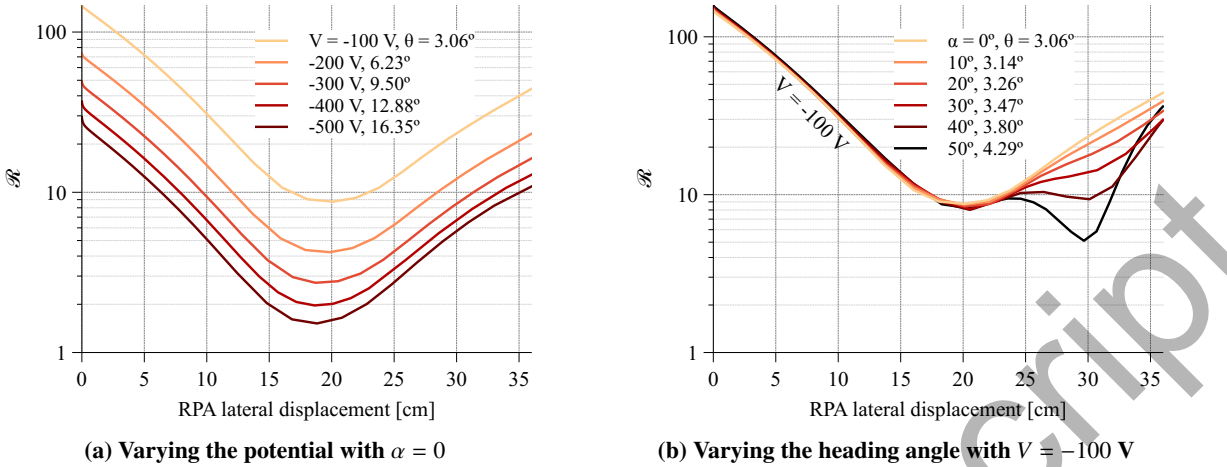


Fig. 8 Validation metrics \mathcal{R} and θ as a function of the electrode potential and heading angle

is smaller than the one reported in Fig. 5. This is due to limitations imposed by the power density threshold of the phosphor screen and the effective aperture of the RPA[‡].

The influence of the electrode rotation angle α on the beam deflection and spot shape is also explored in Fig. 6 for $V = -100 \text{ V}$ and $\alpha = 10^\circ$ to 50° . Although the beam is deflected and the cross section is modified, these effects are much less pronounced than in Fig. 4, implying that the \mathcal{R} metric is significantly larger. In other words, the uncoupled model is far more appropriate for this case.

The framework of analysis introduced in Sec. II is not designed to predict the elongation of the beam cross-section, but still gives accurate estimations for those cases where the beam deflection angle is small. In order to evaluate the validity metrics defined in Sec. II.C.4, the experimental setup is reproduced with a 934-spheres MSM representation of the spacecraft-like electrode. The result is shown in Fig. 7 for an electrode potential of -500 V , that corresponds to the case in Fig. 4f, and a beam expansion angle $\delta = 2.5^\circ$.

The validity metrics \mathcal{R} and θ are reported in Fig. 8a as a function of the electrode potential V and in Fig. 8b in terms of the electrode rotation angle α . An increase in the electrode potential decreases the minimum \mathcal{R} value and increases the deflection angle θ , reaching $\sim 3^\circ$ and 9.5° , respectively, for the limit case of -300 V . Larger values lead to significant beam cross-section deformations, as shown in Figs. 4e-4f. Similarly, the rotation of the electrode creates a second minimum in the \mathcal{R} plot (i.e. a second maximum in the electromagnetic force), but since this minimum is larger than in the -200 V case, its effects on the beam cross-section are less significant. Due to the large beam expansion angle δ , the magneto-electrostatic repulsion between electrons plays virtually no role in the expansion dynamics of the beam.

The experiment demonstrates the appropriateness of the expansion/deflection decoupling when the validation metrics \mathcal{R} and θ adopt sufficiently large values. In such cases, the beam cross-section becomes practically independent of the

[‡]The variations in light intensity at the phosphor screen are caused by the Electron-Beam-Induced-Deposition (EBID) of carbon and heavy molecules over the surface, and not by variations in the distribution of electrons in the beam cross-section.

external electromagnetic force. Although the assumptions of the model significantly constraint its validity range, it is precisely in the spacecraft charging scenario where this computationally efficient framework can be better exploited.

IV. Uncertainty in active spacecraft charging scenario

A. Problem statement

Once the validity of the beam model has been contrasted with experimental observations, the base scenario of analysis is introduced in Fig. 9. The GOES-R^{\$} and SSL-1300[¶] spacecraft MSM models are shown together with the e^- beam centroid evolution in the global reference system $\{\hat{x}, \hat{y}, \hat{z}\}$. The target spacecraft (-2.5 V) is negatively charged with respect to the servicer (0 kV) due to the current unbalance induced by the electron beam, generating a net electrostatic force that tends to deflect and slow down the 5 keV, 10 μ A electrons from $4.2 \cdot 10^7$ m/s to $3.2 \cdot 10^7$ m/s. The electron beam energy must be larger than the absolute potential difference to allow the electrons to reach the target surface. The \mathcal{R} parameter depends quadratically on the propagation speed and approximately linearly on the beam energy (see Eq. (16)), and hence the physical model here adopted is particularly well suited for high beam energy applications.

The trade-off between beam energy and spacecraft potential is analyzed in Fig. 10 by comparing the validation metrics along the beam trajectory in three different scenarios. As expected, an increase in beam energy leads to larger \mathcal{R} and smaller θ values, while a decrease in the target spacecraft potential has the opposite effect. In the nominal case ($E_b = 5$ keV, $V = -2.5$ kV), a deflection angle $\theta = 5.33^\circ$ and a minimum $\mathcal{R} = 4$ are reached, satisfying the validity

^{\$}<https://www.goes-r.gov/spacesegment/spacescraft.html> (Consulted on: 01/06/2021)

[¶]http://sslmda.com/html/1300_series_platform.php (Consulted on: 01/06/2021)

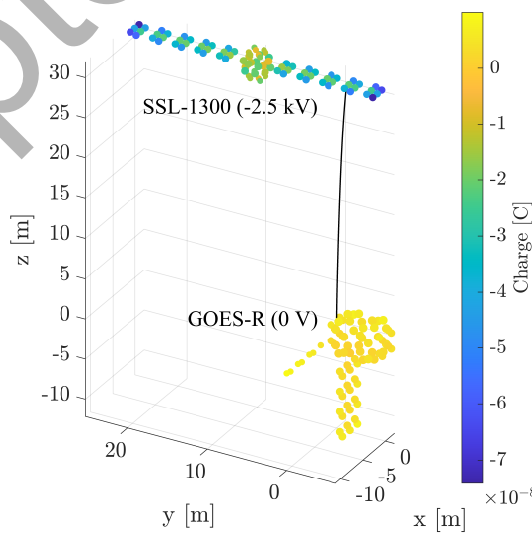


Fig. 9 Geometry of the 2-SC problem for the basic simulation parameters (see Table 1).

range of the model. These values are analogous, in terms of \mathcal{R} and θ , to the experimental -200 V case pictured in Fig. 4c and analyzed in Fig. 8.

Figure 11 explores the beam expansion dynamics for different deflection angles. When a stream of collimated electrons ($\delta = 0$) exits the gun, the magneto-electrostatic repulsion expands the beam radius from 2.5 to 40 mm in the 30 m flight. The trajectory of those electrons is non-linear, but as the initial δ angle is increased, a linear expansion is achieved. This qualitatively different behavior reflects the existence of *repulsive* and *inertial* expansion regimes. Although in the second case the expansion dynamics become practically irrelevant, a larger beam-target intersection is also obtained. This may not be convenient for the characterization of the target.

A discretization of 50 radial points is employed to model the expansion process, deviating less than a 0.01% from a 200-points model in the worst-case collimated beam regime. An MSM model with 172 spheres is applied to the deflection problem, resulting in errors below 5 cm in the final beam centroid position with respect to a high-fidelity 1976 spheres MSM simulation. These results are acceptable for the problem here discussed.

B. Uncertainty quantification analysis

The model built in Sec. II is, because of its computational efficiency, particularly well suited to quantify the uncertainty in the beam-target intersection position in an active spacecraft charging scenario. The analysis is designed from the perspective of a servicing spacecraft that seeks to steer the beam toward a particular spot of the target. A total of 702 uncertain variables are considered, with 688 being associated to the MSM spheres that approximate the charge distribution of the two-spacecraft system. The list of input variables and their distribution is detailed in Table 1. The outputs of the analysis are (i) the radius of the beam cross section at the end of flight, (ii) the centroid landing position in the target plane, which is perpendicular to the line of sight between both spacecraft, (iii) the landing energy, and (iv) the time of flight.

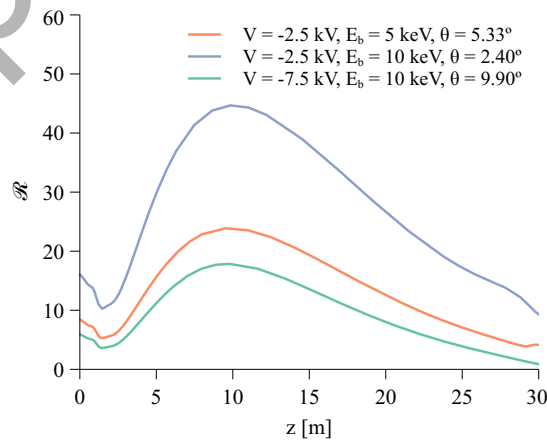


Fig. 10 Validation metrics \mathcal{R} and θ as a function of the target spacecraft potential V and beam energy E_b for the nominal active spacecraft charging scenario.

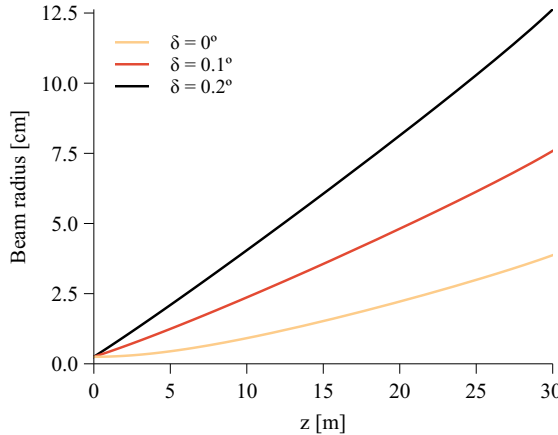


Fig. 11 Beam radius evolution as a function of divergence angle for the nominal active spacecraft charging scenario.

Table 1 Uncertainty analysis parameters

Variable	Distribution	Mean	STD	Unit
Beam current (I_b)	Normal	10	0.1	μA
Beam energy (E_b)	Normal	5	0.05	keV
Initial divergence angle (δ)	Uniform	0.1	Lims: [0, 0.2]	deg
Initial particle density STD (σ_p)	Normal	0.83	0.083	mm
Servicer potential (V_{ser})	Normal	0	0.05	kV
Servicer, Euler-313 ($\psi_{\text{ser}}, \theta_{\text{ser}}, \phi_{\text{ser}}$)	Normal	[0,90,0]	[0.1,0.1,0.1]	deg
Target potential (V_{tar})	Normal	-2.5	0.25	kV
Target, Euler-313 ($\psi_{\text{tar}}, \theta_{\text{tar}}, \phi_{\text{tar}}$)	Normal	[0,180,0]	[5,5,5]	deg
Relative Position (r_x, r_y, r_z)	Normal	[0,10,32]	[0.5,0.5,1]	m
Capacitances (x172)	Normal	Dataset	1%	C
Spheres pos. (x516)	Normal	Dataset	1%	m
Initial beam radius	Fixed	2.5	0	mm

Due to the large number of parameters and reduced computational cost of the simulation, a Monte Carlo analysis is chosen over other uncertainty quantification methods. The relative influence of each input parameter on the output metrics is measured by means of sensitivity indices, computed with a Fourier Amplitude Sensitivity Testing (FAST) suite[¶] from Ref. 45.

C. Results

The Monte Carlo analysis is carried out with 10^4 random realizations generated from the distributions reported in Table 1, which are conservative estimations of the different sources of error. Each simulation takes approximately 0.6 s after parallelizing the code with 7 CPU threads in Matlab 2021 (Intel Core i7-7820HQ CPU at 2.90 GHz, 32 Gb RAM).

[¶]<https://www.mathworks.com/matlabcentral/fileexchange/40759-global-sensitivity-analysis-toolbox> (Consulted on: 01/06/2021)

The solution converges in mean and variance for the expansion and deflection problems.

Results in Fig. 12 depict the Probability Density Functions (PDFs) of the model outputs: (a) final beam radius $R_{b,f}$, (b) final centroid position $p_{x,f}$ and $p_{y,f}$, (c) time of flight t_f , and (d) final beam energy $E_{b,f}$. The first follows a quasi-uniform distribution, clearly influenced by the uniform sampling of the initial deflection angle δ , and spans from 4 to 13 cm. These expansion values, computed for $\delta \subseteq [0^\circ, 0.2^\circ]$, are small in comparison with the spread of the beam centroid shown in Fig. 12b, where the target $[0.11, -1.26]$ m is marked as a red cross. The landing positions follow a multi-Gaussian distribution with mean $[0.07, -1.20]$ m and covariance $[0.20, -0.006; -0.006, 0.28]$ m². This implies that the beam centroid has a 93.9% probability of intercepting the SSL-1300 solar panel, represented as a rectangle in the figure, while the chances of hitting a 20 cm diameter circle surrounding the target are just a 0.3%. The time of flight PDF is represented in Fig. 12c and follows a log-normal distribution with logarithmic mean $14.07 \mu\text{s}$ and variance $2.14 \cdot 10^{-4} \mu\text{s}^2$. This result is relevant for applications employing pulsed beam modulations to filter the returning secondary electron flux from the target. Modulated electron beams have been employed in previous space instruments, such as the Electron Drift Instrument of MMS [19]. Finally, the landing energy PDF is shown in Fig. 12d and fitted with a Weibull distribution (scale 3309.98, shape 9.97) with mean 3148.55 keV and variance 144294 keV². The landing energy determines the SE yield, and is hence important for defining the resulting SE flux [1]. It also determines the X-ray spectrum profile and intensity [46].

In order to determine the influence of each input on the outcomes reported in Fig. 12, a Fourier Amplitude Sensitivity Testing (FAST) Global Sensitivity Analysis (GSA) is conducted. The analysis is limited to the 15 non-MSM inputs in Table 1 to minimize its computational cost. Although 688 MSM variables are removed, Table 2 shows how the total variances remain practically identical, denoting that such uncertain inputs have a negligible effect in the final distributions.

Table 3 reports the sensitivity coefficients for 10^4 realizations. The five outputs of the model (final beam radius $E_{b,f}$, beam-target intersection coordinates $p_{x,f}$ and $p_{y,f}$, final energy $E_{b,f}$, and time of flight t_f) are listed in the rows, while the inputs are shown in the columns. Bold fonts are employed to highlight the largest sensitivities, showing that each output variance can be almost completely explained with less than two inputs. For instance, the final beam radius is mainly dependent on the initial divergence angle, while the final positions are related to the uncertainties in

Table 2 Comparison of output variances between the full 702 parameters and the reduced 15 parameters MC analyses

	$V(R_{b,f})$ [m ²]	$V(p_{x,f})$ [m ²]	$V(p_{y,f})$ [m ²]	$V(E_{b,f})$ [keV ²]	$V(t_f)$ [s ²]
Full	6.830e-4	0.204	0.276	1.387e5	1.301e-16
Reduced	6.790e-4	0.203	0.269	1.456e5	1.319e-16

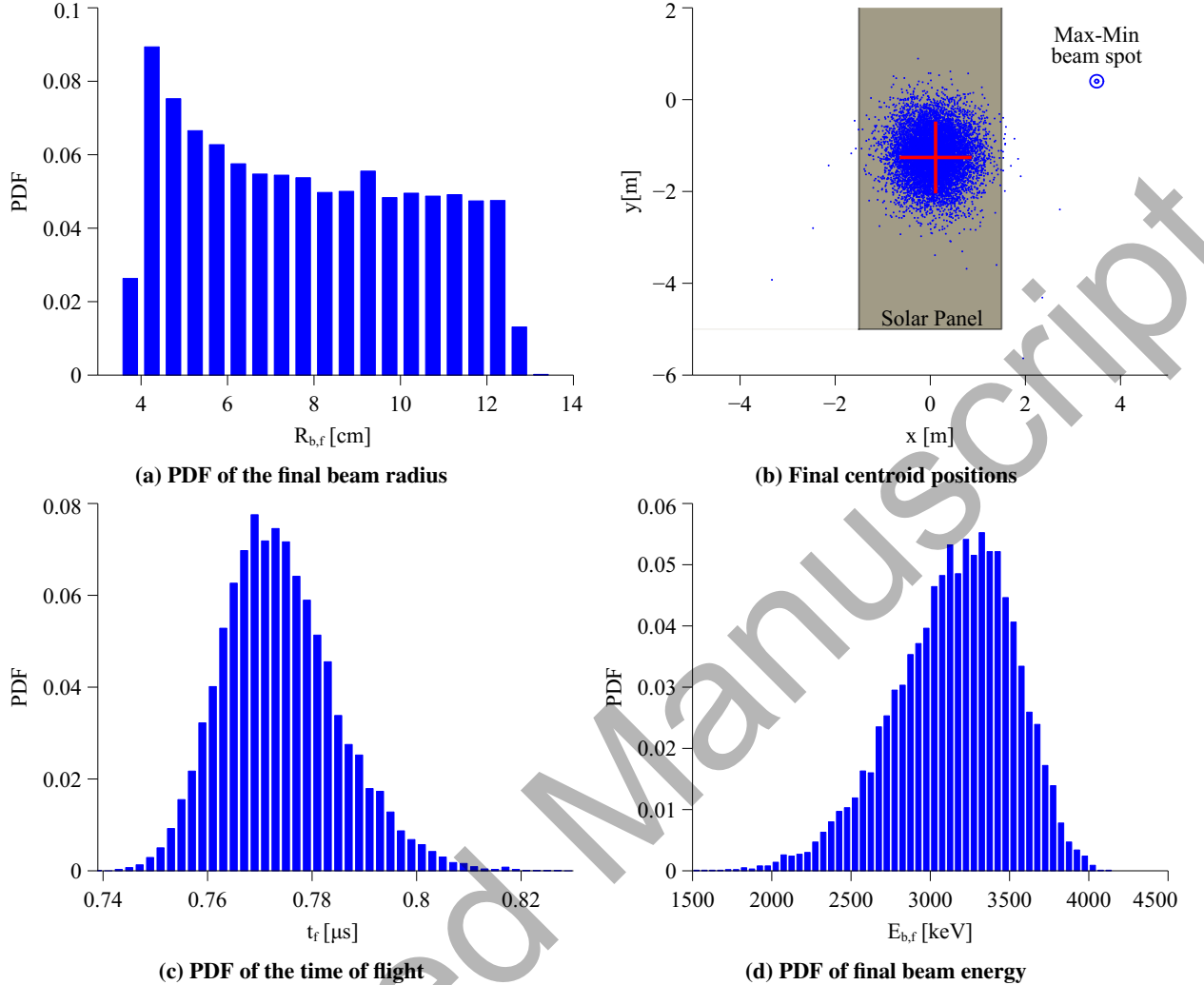


Fig. 12 Result of the Monte Carlo simulation

their corresponding relative spacecraft position component. The output $p_{y,f}$ is also dependent on the target potential, which promotes the lateral deflection of the beam, as shown in Fig. 4. Although the results seem to indicate that the variance in $p_{x,f}$ is also explained by the beam current I_b , this should be attributed to numerical errors, because the model uncouples the expansion and deflection problems. The final beam energy $E_{b,f}$ and time of flight t_f are depend on the initial beam energy E_b and target spacecraft potential V_{tar} , whose relative influence is strongly influenced by the uncertainty bands selected in Table 1. The attitude of each spacecraft does not seem to have a large influence in any output variable; however, this is caused by the small attitude disturbance angles selected in Table 1, which would increase with less accurate attitude determination sensors.

It should be noted that, among the most influential input parameters, only the target potential and relative positions are not predefined. An obvious conclusion is that the targeting of specific regions is limited by the accuracy in the measurement of the relative position between the two spacecraft. Although this problem may be addressed with

Table 3 Normalized sensitivity indices from FAST sensitivity analysis with 15 inputs and 5 outputs. The values are scaled by a factor of 10 for convenience.

	I_b	E_b	σ_b	V_{tar}	V_{ser}	r_x	r_y	r_z	ϕ_{tar}	θ_{tar}	ψ_{tar}	ϕ_{ser}	θ_{ser}	ψ_{ser}	δ
$R_{b,f}$	0.053	0.112	0.011	0.306	0.044	0.009	0.019	0.121	0.005	0.001	0.015	0.056	0.318	0.365	8.563
$p_{x,f}$	1.208	0.204	0.009	0.016	0.004	8.284	0.001	0.003	0.233	0.002	0.005	0.002	0.025	0.002	0.002
$p_{y,f}$	0.004	0.030	0.033	1.550	0.354	0.003	7.888	0.109	0.001	0.003	0.001	0.003	0.020	0.001	0.001
$E_{b,f}$	0.056	1.541	0.021	7.122	0.554	0.071	0.126	0.226	0.117	0.138	0.006	0.005	0.005	0.013	0.001
t_f	0.028	3.524	0.005	4.661	0.760	0.006	0.024	0.741	0.010	0.238	0.001	0.000	0.001	0.001	0.001

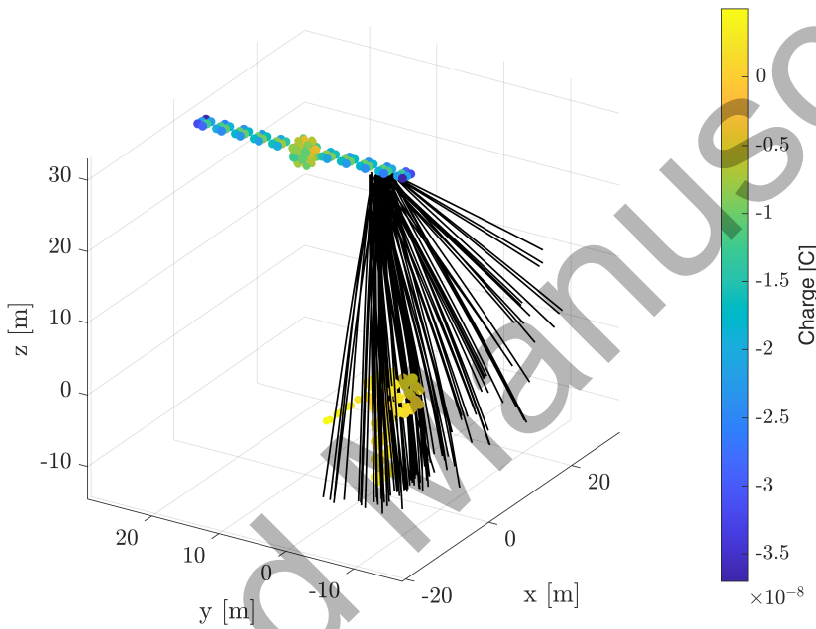


Fig. 13 Trajectory of 100 secondary electrons generated in the beam-target intersection region described by the Monte Carlo analysis in Fig. 12b.

better sensing equipment, the strong influence of the target potential raises additional issues. In order to obtain a first measurement, the electron beam needs to intercept the target, but such interception can only be guaranteed if an estimate of V_{tar} is available. The problem may be solved by temporarily increasing the beam expansion angle δ to irradiate larger areas, enhancing the chances of collision, or by employing a more directive beam with higher energy E_b . An X-ray sensor oriented toward the irradiated region would then be used to obtain the first target voltage estimation, which would then be followed by more accurate SE estimations.

However, the availability of target potential measurements using the SE method, which is significantly more accurate than the X-ray approach [13], is strongly dependent on the geometry of the system [14]. The spatial distribution reported in Fig. 12b for the beam-target intersection has a critical influence on the flux of SEs. Figure 13 depicts the trajectories of 100 SEs uniformly generated in a circle with 1.5 m radius (3σ interval) and whose center matches the origin of the

Monte Carlo final beam centroid distribution ($x = 0.07$ m, $y = -1.20$ m, $z = 30$ m). Since they are born with energies of the order of just a few eV [47], SEs are assumed to start their trajectory with zero velocity. The SEs are able to reach the servicer only when the beam hits a very specific area of the target, so it can be readily concluded that a limited subspace of the Monte Carlo solution domain will be detectable. That is, an RPA mounted in the servicer and aimed at a suitable target region is not guaranteed to detect SEs with the statistical distributions reported in Table 1, concluding that the combination of X-ray and SE measurements is necessary to ensure a robust and accurate estimation of the target spacecraft potential. A feedback control loop may be employed to actively steer the beam and guarantee the measurement of SEs, following an implementation analogous to the Electron Drift Instrument of MMS [19].

V. Conclusions

This paper introduces a quasi-analytical electron beam model that achieves a great computational efficiency by decoupling the beam expansion and deflection processes. Although this choice restricts the range of application of the simulation framework, experimental observations in the ECLIPS Space Environments Simulation Facility [44] validate its use in active spacecraft charging problems, where small deflection angles and radial expansions are expected.

The model is employed to quantify the uncertainty of key metrics in a representative active charging scenario. The sensitivity of the beam dynamics to a characteristic set of input parameters is studied by means of Monte Carlo simulations. Although the electron beam centroid is shown to hit the target spacecraft with a 93.85% chance, this happens within a large $\pm 3\sigma$ Gaussian interval of 3 m around the target. A FAST sensitivity analysis shows that the relative spacecraft position and target spacecraft potential account for most of the variance. Furthermore, only a limited number of solutions ensure that the resulting SEs reach an hypothetical RPA mounted on the servicer, implying that combined X-ray and SE potential sensing methods are not only desired, but actually required for a robust and accurate target potential estimation. This setup would benefit from a closed control loop to guarantee the detectability of SEs in uncertain environments.

Acknowledgments

The authors thank Prof. Alireza Doostan for his assistance in the development of the uncertainty quantification analysis, and Dr. Miles Bengtson and Dr. Kieran Wilson for fruitful discussions on the setup and operation of the vacuum chamber experiment. This work was partially supported by U.S. Air Force Office of Scientific Research under grant FA9550-20-1-0025 and the *La Caixa* Foundation (ID 100010434), under agreement LCF/BQ/AA18/11680099.

References

- [1] Bengtson, M. T., Wilson, K. T., and Schaub, H., “Experimental Results of Electron Method for Remote Spacecraft Charge Sensing,” *Space Weather*, Vol. 18, No. 3, 2020, pp. 1–12. <https://doi.org/10.1029/2019SW002341>.

- [2] Wilson, K., and Schaub, H., "X-Ray Spectroscopy for Electrostatic Potential and Material Determination of Space Objects," *IEEE Transactions on Plasma Science*, Vol. 47, No. 8, 2019, pp. 3858–3866. <https://doi.org/10.1109/TPS.2019.2910576>.
- [3] Wilson, K. T., Bengtson, M. T., and Schaub, H., "X-ray Spectroscopic Determination of Electrostatic Potential and Material Composition for Spacecraft: Experimental Results," *Space Weather*, Vol. 18, No. 4, 2020, pp. 1–10. <https://doi.org/10.1029/2019SW002342>.
- [4] Bengtson, M., Hughes, J., and Schaub, H., "Prospects and Challenges for Touchless Sensing of Spacecraft Electrostatic Potential Using Electrons," *IEEE Transactions on Plasma Science*, Vol. 47, No. 8, 2019, pp. 3673–3681. <https://doi.org/10.1109/TPS.2019.2912057>.
- [5] Casale, F., Schaub, H., and Douglas Biggs, J., "Lyapunov Optimal Touchless Electrostatic Detumbling of Space Debris in GEO Using a Surface Multisphere Model," *Journal of Spacecraft and Rockets*, Vol. 58, No. 3, 2021, pp. 764–778. <https://doi.org/10.2514/1.A34787>.
- [6] Hughes, J., and Schaub, H., "Prospects of Using a Pulsed Electrostatic Tractor With Nominal Geosynchronous Conditions," *IEEE Transactions on Plasma Science*, Vol. 45, No. 8, 2017, pp. 1887–1897. <https://doi.org/10.1109/TPS.2017.2684621>.
- [7] Bengtson, M., Wilson, K., Hughes, J., and Schaub, H., "Survey of the electrostatic tractor research for reorbiting passive GEO space objects," *Astrodynamic*, Vol. 2, No. 4, 2018, pp. 291–305. <https://doi.org/10.1007/s42064-018-0030-0>.
- [8] Hughes, J. A., and Schaub, H., "Electrostatic Tractor Analysis Using a Measured Flux Model," *Journal of Spacecraft and Rockets*, Vol. 57, No. 2, 2020, pp. 207–216. <https://doi.org/10.2514/1.A34359>.
- [9] Schaub, H., Parker, G. G., and King, L. B., "Challenges and Prospect of Coulomb Formations," *Journal of the Astronautical Sciences*, Vol. 52, No. 1–2, 2004, pp. 169–193. <https://doi.org/10.1007/BF03546427>.
- [10] Wilson, K., and Schaub, H., "Impact of Electrostatic Perturbations on Proximity Operations in High Earth Orbits," *Journal of Spacecraft and Rockets*, Vol. 0, No. 0, 2021, pp. 1–10. <https://doi.org/10.2514/1.A35039>.
- [11] Wilson, K., Romero-Calvo, A., and Schaub, H., "Constrained Guidance for Spacecraft Proximity Operations Under Electrostatic Perturbation," *Journal of Spacecraft and Rockets*, 2021. *under review*.
- [12] Schaub, H., and Moorer, D. F., "Geosynchronous Large Debris Reorbiter: Challenges and Prospects," *The Journal of the Astronautical Sciences*, Vol. 59, No. 1, 2012, pp. 161–176. <https://doi.org/10.1007/s40295-013-0011-8>.
- [13] Wilson, K. T., Bengtson, M., and Schaub, H., "Remote Electrostatic Potential Sensing for Proximity Operations: Comparison and Fusion of Methods," *Journal of Spacecraft and Rockets*, 2021. *under review*.
- [14] Bengtson, M. T., and Schaub, H., "Electron-Based Touchless Potential Sensing of Shape Primitives and Differentially-Charged Spacecraft," *Journal of Spacecraft and Rockets*, Vol. 0, No. 0, 2021, pp. 1–11. <https://doi.org/10.2514/1.A35086>.
- [15] Olsen, R., and Cohen, H., "Electron beam experiments at high altitudes," *Advances in Space Research*, Vol. 8, No. 1, 1988, pp. 161 – 164. [https://doi.org/10.1016/0304-3886\(87\)90085-4](https://doi.org/10.1016/0304-3886(87)90085-4).

- [16] Melzner, F., Metzner, G., and Antrack, D., “The GEOS electron beam experiment,” *Space Science Instrumentation*, Vol. 4, 1978, pp. 45–55.
- [17] Paschmann, G., Boehm, M., Höfner, H., Frenzel, R., Parigger, P., Melzner, F., Haerendel, G., Kletzing, C. A., Torbert, R. B., and Sartori, G., “The Electron Beam Instrument (F6) on Freja,” *Space Science Reviews*, Vol. 70, No. 3, 1994, pp. 447–463. <https://doi.org/10.1007/BF00756881>.
- [18] Paschmann, G., Melzner, F., Frenzel, R., Vaith, H., Parigger, P., Pagel, U., Bauer, O. H., Haerendel, G., Baumjohann, W., Scopke, N., Torbert, R. B., Briggs, B., Chan, J., Lynch, K., Morey, K., Quinn, J. M., Simpson, D., Young, C., Mcilwain, C. E., Fillius, W., Kerr, S. S., Mahieu, R., and Whipple, E. C., “The Electron Drift Instrument for Cluster,” *Space Science Reviews*, Vol. 79, No. 1, 1997, pp. 233–269. <https://doi.org/10.1023/A:1004917512774>.
- [19] Torbert, R. B., Vaith, H., Granoff, M., Widholm, M., Gaidos, J. A., Briggs, B. H., Dors, I. G., Chutter, M. W., Macri, J., Argall, M., Bodet, D., Needell, J., Steller, M. B., Baumjohann, W., Nakamura, R., Plaschke, F., Ottacher, H., Hasiba, J., Hofmann, K., Kletzing, C. A., Bounds, S. R., Dvorsky, R. T., Sigsbee, K., and Kooi, V., “The Electron Drift Instrument for MMS,” *Space Science Reviews*, Vol. 199, No. 1, 2016, pp. 283–305. <https://doi.org/10.1007/s11214-015-0182-7>.
- [20] Garrett, H. B., and Whittlesey, A. C., “Spacecraft Design Guidelines,” *Guide to Mitigating Spacecraft Charging Effects*, John Wiley & Sons, Ltd, 2012, Chap. 3, pp. 26–61. <https://doi.org/10.1002/9781118241400.ch3>.
- [21] Olsen, R. C., McIlwain, C. E., and Whipple Jr., E. C., “Observations of differential charging effects on ATS 6,” *Journal of Geophysical Research: Space Physics*, Vol. 86, No. A8, 1981, pp. 6809–6819. <https://doi.org/10.1029/JA086iA08p06809>.
- [22] Grard, R., Knott, K., and Pedersen, “Spacecraft charging effects,” *Space Science Reviews*, Vol. 34, No. 3, 1983, pp. 289–304. <https://doi.org/10.1007/BF00175284>.
- [23] Roeder, J. L., and Fennell, J. F., “Differential Charging of Satellite Surface Materials,” *IEEE Transactions on Plasma Science*, Vol. 37, No. 1, 2009, pp. 281–289. <https://doi.org/10.1109/TPS.2008.2004765>.
- [24] Ferguson, D., White, S., Rast, R., and Holeman, E., “The Case for Global Positioning System Arcing and High Satellite Arc Rates,” *IEEE Transactions on Plasma Science*, Vol. 47, No. 8, 2019, pp. 3834–3841. <https://doi.org/10.1109/TPS.2019.2922556>.
- [25] Manura, D., and Dahl, D., *SIMION (R) 8.1 User Manual*, Rev-5, Adaptas Solutions, LLC, Palmer, MA 01069, 2008. URL <http://simion.com/manual/>.
- [26] Okuda, H., and Berchem, J., “Injection and propagation of a nonrelativistic electron beam and spacecraft charging,” *Journal of Geophysical Research: Space Physics*, Vol. 93, No. A1, 1988, pp. 175–195. <https://doi.org/10.1029/JA093iA01p00175>.
- [27] Okuda, H., and Ashour-Abdalla, M., “Propagation of a nonrelativistic electron beam in three dimensions,” *Journal of Geophysical Research: Space Physics*, Vol. 95, No. A3, 1990, pp. 2389–2404. <https://doi.org/10.1029/JA095iA03p02389>.
- [28] Okuda, H., and Ashour-Abdalla, M., “Injection of an overdense electron beam in space,” *Journal of Geophysical Research: Space Physics*, Vol. 95, No. A12, 1990, pp. 21307–21311. <https://doi.org/10.1029/JA095iA12p21307>.

- [29] Winglee, R. M., "Simulations of pulsed electron beam injection during active experiments," *Journal of Geophysical Research: Space Physics*, Vol. 96, No. A2, 1991, pp. 1803–1817. <https://doi.org/10.1029/90JA02102>.
- [30] Koga, J., and Lin, C. S., "A simulation study of radial expansion of an electron beam injected into an ionospheric plasma," *Journal of Geophysical Research: Space Physics*, Vol. 99, No. A3, 1994, pp. 3971–3983. <https://doi.org/10.1029/93JA02230>.
- [31] Harting, E., and F.H., R., *Electrostatic Lenses*, Elsevier Publishing Company, Amsterdam, 1976.
- [32] Read, F. H., Chalupka, A., and Bowring, N. J., "Charge-tube method for space charge in beams," *Charged Particle Optics IV*, Vol. 3777, edited by E. Munro, International Society for Optics and Photonics, SPIE, 1999, pp. 184 – 191. <https://doi.org/10.1117/12.370129>.
- [33] Renau, A., Read, F. H., and Brunt, J. N. H., "The charge-density method of solving electrostatic problems with and without the inclusion of space-charge," *Journal of Physics E: Scientific Instruments*, Vol. 15, No. 3, 1982, pp. 347–354. <https://doi.org/10.1088/0022-3735/15/3/025>.
- [34] Humphries, S., *Charged Particle Beams*, Wiley, 1990. Chapter 5: Introduction to Beam-Generated Forces.
- [35] Gendrin, R., "Initial expansion phase of an artificially injected electron beam," *Planetary and Space Science*, Vol. 22, No. 4, 1974, pp. 633 – 636. [https://doi.org/10.1016/0032-0633\(74\)90097-X](https://doi.org/10.1016/0032-0633(74)90097-X).
- [36] Stevenson, D., and Schaub, H., "Multi-Sphere Method for modeling spacecraft electrostatic forces and torques," *Advances in Space Research*, Vol. 51, No. 1, 2013, pp. 10 – 20. <https://doi.org/10.1016/j.asr.2012.08.014>.
- [37] Lewellen, J. W., Buechler, C. E., Carlsten, B. E., Dale, G. E., Holloway, M. A., Patrick, D. E., Storms, S. A., and Nguyen, D. C., "Space-Borne Electron Accelerator Design," *Frontiers in Astronomy and Space Sciences*, Vol. 6, 2019, p. 35. <https://doi.org/10.3389/fspas.2019.00035>.
- [38] Lai, S. T., *Fundamentals of Spacecraft Charging: Spacecraft Interactions with Space Plasmas*, Princeton University Press, 2012.
- [39] Smythe, W., *Static and Dynamic Electricity*, 3rd ed., McGraw-Hill, 1968.
- [40] Hughes, J. A., and Schaub, H., "Heterogeneous Surface Multisphere Models Using Method of Moments Foundations," *Journal of Spacecraft and Rockets*, Vol. 56, No. 4, 2019, pp. 1259–1266. <https://doi.org/10.2514/1.A34434>.
- [41] Qin, H., Zhang, S., Xiao, J., Liu, J., Sun, Y., and Tang, W. M., "Why is Boris algorithm so good?" *Physics of Plasmas*, Vol. 20, No. 8, 2013, p. 084503. <https://doi.org/10.1063/1.4818428>.
- [42] Shampine, L. F., and Reichelt, M. W., "The MATLAB ODE Suite," *SIAM Journal on Scientific Computing*, Vol. 18, No. 1, 1997, pp. 1–22. <https://doi.org/10.1137/S1064827594276424>.
- [43] Bengtson, M. T., "Electron Method for Touchless Electrostatic Potential Sensing of Neighboring Spacecraft," Ph.D. thesis, University of Colorado Boulder, 2020. URL <http://hanspeterschaub.info/Papers/grads/MilesBengtson.pdf>.

- [44] Wilson, K., Romero-Calvo, A., Bengtson, M., Hammerl, J., Maxwell, J., and Schaub, H., "Development and Characterization of the ECLIPS Space Environments Simulation Facility," *Acta Astronautica*, 2021. *under review*.
- [45] Cannavó, F., "Sensitivity analysis for volcanic source modeling quality assessment and model selection," *Computers & Geosciences*, Vol. 44, 2012, pp. 52 – 59. <https://doi.org/10.1016/j.cageo.2012.03.008>.
- [46] Wilson, K. T. H., and Schaub, H., "An X-ray Spectroscopic Approach to Remote Space Object Potential Determination: Experimental Results," *AIAA SciTech*, Orlando, Florida, 2020. <https://doi.org/10.2514/6.2020-0049>.
- [47] Chung, M. S., and Everhart, T. E., "Simple calculation of energy distribution of low-energy secondary electrons emitted from metals under electron bombardment," *Journal of Applied Physics*, Vol. 45, No. 2, 1974, pp. 707–709. <https://doi.org/10.1063/1.1663306>.

Accepted Manuscript